High-resolution methane mapping with the EnMAP satellite imaging spectroscopy mission

Javier Roger [a,*], Itziar Irakulis-Loitxate [a,b], Adriana Valverde [a], Javier Gorroño [a], Sabine Chabrillat [c,d], Maximilian Brell [c], Luis Guanter [a,e]

[a]*Research Institute of Water and Environmental Engineering (IIAMA), Universitat Politècnica de València (UPV), 46022, Valencia, Spain*
[b]*International Methane Emission Observatory (IMEO), United Nations Environment Programme, Paris, France*
[c]*Helmholtz Centre Potsdam – GFZ German Research Centre for Geosciences, Telegrafenberg, 14473 Potsdam, Germany*
[d]*Leibniz University Hannover, Institute of soil science, Herrenhäuser Str. 2, 30419 Hannover, Germany*
[e]*Environmental Defense Fund, Reguliersgracht 79, 1017 LN Amsterdam, The Netherlands*

Abstract

Methane mitigation from anthropogenic sources such as fossil fuels and waste management has been found as one of the most promising strategies to curb global warming in the near future. Satellite-based imaging spectrometers have demonstrated to be well-suited to detect and quantify these emissions at high spatial resolution. These instruments produce so-called hyperspectral data cubes of the solar radiation reflected by the Earth, measuring in the 400-2500 nm spectral range, with a spectral sampling of 5-15 nm and a spatial sampling of 30-60 m. Methane concentration enhancement maps are generated from those data cubes by leveraging spectral channels across the 2300 nm methane absorption window. The relatively high spatial resolution of the resulting methane maps allows for the detection and attribution of plumes to sources. The PRISMA satellite mission (ASI, Italy) has been extensively used in the last years for this application. The recently-launched EnMAP mission (DLR/GFZ, Germany) presents similar spatial and spectral characteristics to PRISMA (30 m spatial resolution, 30 km swath, about 8 nm spectral sampling at 2300 nm) and can a priori thus be used for methane mapping as well. In this work, we investigate the potential and limitations of EnMAP for methane remote sensing, using PRISMA as a benchmark. First, we analyze the spectral and radiometric performance of EnMAP in the 2300 nm region used for methane retrievals, which includes parameters such as spectral uniformity and resolution and the signal-to-noise ratio (SNR). Our results show that in desertic areas at 2300 nm, EnMAP spectral resolution is about 2.7 nm smaller than in PRISMA and the SNR values are approximately twice as large, which leads to a higher sensitivity to methane that improves retrieval performance. This finding is illustrated by several show cases of methane plumes from different sources around the world with flux rate values ranging approximately from 1 to 20 t/h. We show plumes from sectors such as onshore oil and gas and coal mining, but also from more challenging sectors to detect such as landfills and offshore oil and gas. From the latter we detected two plumes with an unprecedented flux rate of about 1 t/h, which suggests that the detection limit in offshore areas can be significantly low under favorable conditions.

Key words: EnMAP, methane, matched-filter, retrieval, plumes

1. Introduction

Methane (CH_4) plays an important role to curb global warming (Ming et al., 2022). This is due to its relatively short life in the atmosphere ($\sim$12 years) and because its global warming potential in 20 years is 84 times higher than for carbon dioxide (CO_2) (Myhre et al., 2013). Methane anthropogenic emissions are mainly originated from agriculture ($\sim$40%), waste management ($\sim$20%), and fossil fu-
els ($\sim$35%). The latter includes the oil and gas (O&G) industry and coal mining, which have have been identified as the most feasible sectors for methane mitigation (UNEP, 2021). A relevant fraction of the emissions from these sectors are originated from point-sources (Omara et al., 2022; Duren et al., 2019) such as pipeline leaks and venting shafts, which generates more concentrated methane plumes than area-sources such as landfills.

The greater concentration of methane in plumes from point-sources in addition to making them higher pollutants and high targets for mitigation, make them to be more suitable for detection from space-borne instruments. Identify-

ing and monitoring these sources from satellite is key for the creation of a methane emission mitigation plan and imaging spectrometers have proven instrumental in this task (Irakulis-Loitxate et al., 2021). Because of the high spatial resolution of these instruments, emissions detected in the retrieved methane concentration maps can be attributed to their sources (Irakulis-Loitxate et al., 2022b). This can lead to the characterization of super-emitters and other active sources that can guide mitigation (Zavala-Araiza et al., 2017).

Imaging spectrometers measure radiance at hundreds of spectral bands in the visible and near infrared (VNIR: 400-1000 nm) and shortwave infrared (SWIR: 1000-2500 nm), which allows to recreate the radiance spectra along these wavelengths. In the SWIR we can find a weaker methane absorption window around 1700 nm and a stronger one around 2300 nm. These windows can be used to characterize methane and therefore to detect emissions.

Currently, there are some operative open-data satellite-based imaging spectrometers such as the Italian PRISMA (PRecursore IperSpettrale della Missione Applicativa) mission (Loizzo et al., 2018), the German EnMAP (German Environmental Mapping and Analysis Program) mission (Guanter et al., 2015), and NASA'S EMIT (Earth Surface Mineral Dust Source Investigation) mission (Green, 2021). EMIT operates differently currently focusing in arid and semi-arid regions with no tasking and a spatial resolution and swath of 60 m and 80 km, respectively. On the other hand, both EnMAP and PRISMA operate with tasking, have a 30 m of spatial resolution, a swath of 30 km and they present similar spectral resolution and sampling. While PRISMA has already shown its capability to detect methane emissions (Guanter et al., 2021; Irakulis-Loitxate et al., 2021; Joyce et al., 2022), EnMAP has recently become operational (since November 2022) and still was not studied for its capability for methane mapping.

In this work, we will analyze the spectral and radiometric performance of EnMAP in the 2300 nm window used for methane retrievals, using PRISMA as a benchmark to assess the added-value of EnMAP for methane mapping. We will show methane plumes around the world detected with EnMAP datasets in the onshore O&G industry and coal mining areas, but also in more difficult sites to detect methane emissions such as offshore O&G platforms and landfills.

2. Materials and Methods

2.1. Matched-filter based methane retrieval method

Methane concentration maps can be retrieved using the matched-filter method. This algorithm models background radiance as a multivariate Gaussian with mean (μ) and covariance (Σ), assuming a sufficiently homogeneous dataset that exhibits methane enhancement sparsity. Then, shifts from the characterized background radiance are related to
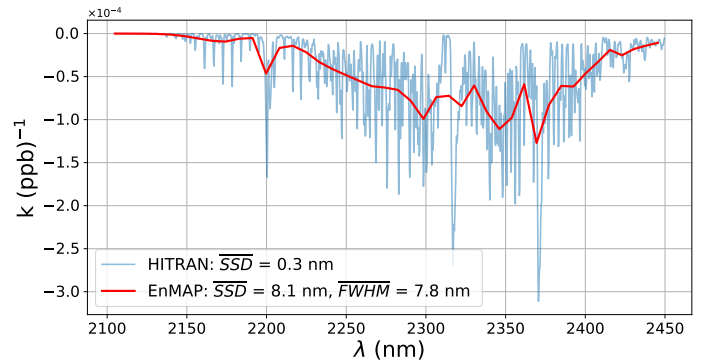

Fig. 1. Unit methane absorption (k) spectra for an EnMAP dataset in the 2300 nm methane absorption window. We difference the HITRAN original k spectrum (blue) and the one that results from a subsequent convolution to EnMAP features (red). In the 2300 nm window, the original HITRAN mean nominal value for SSD is 0.3 nm, while the EnMAP mean nominal values for FWHM and SSD are 7.8 nm and 8.1 nm, respectively.

methane concentration enhancements (Thompson et al., 2016) according to the following expression

$$x = \mu + \Delta XCH_4 \cdot t \qquad (1)$$

where x is the at-sensor radiance spectrum, t is the target signature that defines the radiance spectrum equivalent to a unit of methane concentration absorption with respect to background, and ΔXCH_4 is the methane concentration enhancement in parts-per-billion (ppb). t results from the product between the background mean and the unit methane absorption (k) spectrum. The latter is deduced using a LookUp Table that relates methane transmittance spectra derived from the HITRAN data base (Gordon et al., 2017) to methane concentration, and that also accounts for the specific angular configuration at measurement time. Maximizing the likelihood of this model (Eismann, 2012), we can find that ΔXCH_4 can be described as follows

$$\Delta XCH_4 = \frac{(x-t)^T \Sigma^{-1} t}{t^T \Sigma^{-1} t} \qquad (2)$$

The matched-filter applied to the 2300 nm window is a common option in literature (Foote et al., 2020; Thompson et al., 2015; Dennison et al., 2013). Therefore, we will apply this methodology to the 2300 nm methane absorption window in the 2100-2450 nm range. Although the 1700 nm absorption window typically presents higher radiance levels, the absorption is considerably weaker in comparison, which results in noisier methane retrievals.

2.2. Methane plume detection and quantification

Similarly to Guanter et al. (2021), once ΔXCH_4 maps are generated we search for plumes by visual inspection according to two principles: a methane plume must come from a potential methane emitting source, and must follow the wind direction. If we detect a potential plume, we decide whether it is a real plume or a false positive following these

principles. First, we check the nature of potential sources by comparison to maps of the spectral radiance from which methane maps are derived and with high-resolution images from Google Earth. Once we verify that it is a potential emitting source, we approximate wind speed to the wind speed at 10 m above the surface (U_{10}) derived from GEOS-FP (Molod et al., 2012) and ERA5 (Hersbach et al., 2018), and we select the one that better matches plume direction. If the plume aligns to wind direction, then we can confirm the potential plume.

The flux rate (Q) represents the amount of methane being emitted by the source per unit time. It is derived from the plume pixels, which are obtained by the mask that results from applying an plume detection algorithm and a subsequent supervised correction. The algorithm typically takes as an input a mask that results from keeping $>2\sigma$ pixel values. Then, a morphology filtering is done in order to discard those clusters not associated to the previously identified plume. Finally, of the remainig clusters we only keep the cluster refering to the already detected plume.

We express Q in tons per hour (t/h) units and it is calculated as in Varon et al. (2018) with the following expression

$$Q = \frac{U_{\text{eff}} \cdot \text{IME} \cdot 3.6}{L} \tag{3}$$

where L (m) is the plume size, derived from the square root of the masked area depicting the plume, IME (kg) is the total excess of methane mass within the plume mask (Frankenberg et al., 2016), and U_{eff} (m/s) is the effective wind speed. Note that the 3.6 factor converts from kg/s to t/h units. U_{eff} is calculated from the U_{10} data using a linear model based on WRF-LES simulations (Varon et al., 2018; Cusworth et al., 2019) compatible with EnMAP features and it is expressed as follows

$$U_{\text{eff}} = 0.34 \cdot U_{10} + 0.44 \tag{4}$$

We assume a 50% of wind speed uncertainty as in Guanter et al. (2021) and calculate the Q uncertainty through the quadratic propagation of the IME and U_{10} uncertainties following Eq.3 and Eq.4.

2.3. EnMAP SWIR spectrometer characterization in the 2300 nm window

The radiometric and spectral performance of the EnMAP SWIR spectrometer will drive the accuracy and precision of methane retrievals. In this study, we aim to further chacracterizing the radiometric and spectral responses of EnMAP in the 2300 nm window and study their impact on methane concentration maps. In the same manner, we will characterize the PRISMA SWIR spectrometer for comparison.

2.3.1. Spectral characterization

At-sensor radiance is transformed into a measurable magnitude following a specific Spectral Response Function (SRF) for each of the spectral bands. The SRF describes the sensitivity of each spectral band to the different wavelengths and can be approximated by a Gaussian shape (Gege et al., 2009), determined by its spectral position (named *central wavelength*), and the Full-Width at Half-Maximum (FWHM). The latter determines the spectral resolution and is indicative of the width of the spectral range in which radiation is convoluted to the spectral band. A low value of FWHM will be more sensitive to sharp radiance features, but it will receive less radiance because of the narrower spectral range. Central wavelengths and FWHM are parameters that are usually attached to EnMAP datasets. Moreover, the Spectral Sampling Distance (SSD) is the spectral distance between central wavelengths of adjacent spectral bands. Low SSD values across the VNIR and SWIR would lead to a great number of spectral bands that altogether could better define radiance spectra.

The swath of a dataset is captured by a 2-D detector array when measuring with a push-broom imaging spectrometer such as EnMAP. In this kind of instruments, we can find optical aberrations that lead to shifts in central wavelength (also known as *spectral smile*) and in FWHM (Guanter et al., 2009). These shifts with respect to the nominal values translate into a defficiency in spectral calibration that disturbs the real values of the SRF parameters. The spectral smile derives in a lack of uniformity across the image, which affects the consistency of data. On the other hand, the spectral resolution is important for methane retrieval methods to properly deal with the sharp methane absorption features (Green, 1998). We will obtain central wavelength and FWHM shifts following a similar procedure to Guanter et al. (2021). We first calculate the average spectrum of each column from a Top-Of-Atmosphere (TOA) radiance dataset. Then we apply an iterative procedure that minimizes the l2-norm of the difference between a modeled radiance and the column averaged radiance. This optimization process is done for each column to fit the central wavelength and FWHM values, which are key in the convolution of variables needed to deduce the modeled radiance. We will focus the calculation in the 2280-2380 nm spectral range, that is located approximately at the center of the 2300 nm methane absorption window.

2.3.2. Radiometric characterization

The SNR reflects the relative proportion between signal and measurement noise. Sufficient high values of SNR would translate into practically insensitive-to-noise results, while lower values of SNR would derive in noisier products. Measurement noise can be expressed by the following expression:

$$\sigma_{\text{MN}} = \sqrt{\sigma_{\text{PS}}^2 + \sigma_{\text{rest}}^2} \tag{5}$$

where σ_{MN} is the total measurement noise, σ_{PS} represents the photon shot noise, and the σ_{rest} indicates the noise equivalent to the joint contribution of other noise sources such as the dark current (Du et al., 2022). Photon shot noise comes from the random nature of radiation, which gener-

ates a fluctuation in the count of the number of photoelectrons at the detector that can be modeled as a Poisson distribution (Luo et al., 2010). Moreover, σ_{PS} is proportional to the square root of radiance, while σ_{rest} is a magnitude independent of radiance. Therefore, given a sufficient high value of radiance, σ_{rest} can become relatively negligible to σ_{PS}. In this case we can assume that σ_{MN} can be approximated to σ_{PS} and consequently SNR would also be proportional to the square root of radiance. Then, we will calculate SNR in datasets with high level of radiance in order to scale this magnitude to different radiance values, which would allow us to compare SNR from different datasets.

To calculate the SNR we will use an algorithm based on a principal component decomposition that allows to isolate measurement noise from surface variability. Note that the decomposition is done for each dataset column in order not to involve disturbing effects such as spectral smile and striping noise. Homogeneous datasets are selected to estimate the SNR because it will facilitate the separation between radiance changes related to surface variability and those coming from measurement noise. Then, after applying a per-column principal component decomposition, we manually select by visual inspection the most common principal component across the columns that transitions from surface related structures to decorrelated noise. Therefore, if we subtract the equivalent to all principal components until the selected one to the original dataset, we will obtain a representative measurement noise dataset. Then, we calculate the covariance matrix (Σ_{Noise}) from the latter and obtain the σ_{MN} values for each spectral band from the square root of the Σ_{Noise} diagonal elements. Finally, SNR spectrum is calculated by dividing the radiance spectrum by the resulting σ_{MN} spectrum. Assuming the SNR proportionality to the square root of radiance, we can deduce the constant factor array that will allow us to scale SNR to other radiance values. At the same radiance levels, those missions whose datasets present higher SNR values will have lower σ_{MN}. As a result, there will be a lower impact on the propagation of measurement noise to methane retrievals, which can be deduced by the following expression (Köhler et al., 2015)

$$\sigma_{RMN} = (t^T \Sigma_{Noise}^{-1} t)^{-1} \qquad (6)$$

where σ_{RMN} is the measurement noise contribution to retrieval. Little difference is found between σ_{RMN} values from different columns and therefore an average value is used as representative of the whole methane retrieval extension.

We also consider the *striping noise*, which may result as a consequence of issues such as slight variations in the radiometric response of each across-track detector element and differences in measuring throughout the whole range of across-track pointing (Tsai and Chen, 2008). We evaluate this effect in order to assess the viability of applying methane retrieval methodologies to the whole dataset at once or in a per-column basis. One effective method to evaluate striping is to calculate the ratio between adjacent spectral bands from datasets from the same site. Because

Table 1
Mission, location, sector where the methane emission was originated, date, and central coordinates from the datasets used in this study. Dates are in YYYY-MM-DD format, and latitude and longitude coordinates (*Lat/Lon*) are in decimal degrees. Datasets with no methane emissions are indicated with − in the *Sector* field.

Mission	Location	Sector	Date	Lat/Lon
PRISMA	Northern State (Sudan)	−	2020-04-01	21.900/28.000
PRISMA	Ekizak (Turkmenistan)	Onshore O&G	2022-09-12	38.631/54.227
EnMAP	Agadez (Niger)	−	2022-07-12	21.328/10.477
EnMAP	Khuzestan (Iran)	Onshore O&G	2022-10-22	30.924/48.382
EnMAP	Khuzestan (Iran)	Onshore O&G	2022-09-21	31.074/48.561
EnMAP	Hassi Messaoud (Argelia)	Onshore O&G	2022-11-17	31.782/5.960
EnMAP	Midland Basin (U.S.)	Onshore O&G	2022-10-11	32.490/-102.159
EnMAP	Shanxi (China)	Coal mining	2022-12-05	36.138/113.103
EnMAP	Gamyshlja-Gunorta (Turkmenistan)	Onshore O&G	2022-10-02	38.415/54.163
EnMAP	Gamyshlja-Gunorta (Turkmenistan)	Onshore O&G	2022-10-06	38.373/54.150
EnMAP	Ekizak (Turkmenistan)	Onshore O&G	2022-10-02	38.685/54.243
EnMAP	Ekizak (Turkmenistan)	Onshore O&G	2022-10-06	38.643/54.233
EnMAP	Gogerendag (Turkmenistan)	Onshore O&G	2022-10-02	38.955/54.324
EnMAP	Gogerendag (Turkmenistan)	Onshore O&G	2022-10-06	38.912/54.317
EnMAP	Gulf of Mexico (U.S.)	Offshore O&G	2022-07-01	29.029/-90.370
EnMAP	Delhi (India)	Landfills	2022-11-29	28.554/77.209

of the low SSD of imaging spectrometers, radiance from adjacent bands would be very similar and therefore the ratios would be close to one. Moreover, we need to isolate striping noise as the only source of deviation from this value so we will compare datasets from the same site in order to avoid surface variability disturbance. Striping noise is spectrally decorrelated, i.e. each band will have its own striping pattern. Therefore, the greater the variability between columns in the adjacent band ratio, the greater the striping noise effect. As the spectral smile, a pronounced striping would disturb the consistency between columns.

2.4. *Imaging spectroscopy data*

In this work we have used L1B and L1 level datasets from EnMAP and PRISMA missions, respectively. We will compare datasets from both missions to assess whether EnMAP represents an improvement in methane concentration mapping. We choose an EnMAP dataset from an Agadez Region (Niger) site and a PRISMA dataset in a Sudan site for most comparisons, both in homogeneous desertic areas with similar radiance levels. However, striping noise comparison is done with an EnMAP and a PRISMA datasets from the same site in the Ekizak O&G field (Turkmenistan) to discard surface variability as a striping causing factor. In addition, a comprehensive search for methane plumes was conducted at a wide variety of potential emitting sites. As a result, here we will illustrate plumes originated in different emission sectors from EnMAP datasets in order to show the detection potential of this mission. We will show datasets from the Ekizak, Gamyshlja Gunorta, and Gogerandag O&G fields in Turkmenistan. Note that methane emissions in some of these fields were already detected in Irakulis-Loitxate et al. (2022b). We will also show datasets from a coal mine site in Shanxi (China), the Hassi Messaoud O&G field in Algeria, a site with a pumping station located in Khuzestan (Iran), the Midland basin part of the Permian Basin (U.S.), an offshore O&G site in the U.S. Gulf of Mexico (GoM), and a Delhi (India) area where the Gazhipur and Okhla landfills are located. In Table 1 we show additional information about every dataset used for this work.

3. Results

3.1. *Performance of the EnMAP SWIR spectrometer in the 2300 nm spectral window*

3.1.1. *Spectral performance*

Figure 2 shows the across-track variation of channel spectral position and FWHM from desertic sites in Sudan (PRISMA) and Niger (EnMAP) in a spectral band around 2298.3 nm, which is representative of the whole 2300 nm absorption window. FWHM values accounting for the across-track variations show that on average EnMAP FWHM at $\sim$ 2300 nm is about 2.7 nm smaller than PRISMA FWHM. Therefore, EnMAP can better sample changes in methane absorption. A lower FWHM would also imply a lower at-sensor radiance and would lead to a greater measurement noise, but this is compensated because of the greater EnMAP SNR (see section 3.1.2.). Moreover, the variation from peak-to-peak $\Delta\lambda$ values is lower for EnMAP (1.3 nm) than for PRISMA (2.8 nm). Therefore, EnMAP will be less sensitive than PRISMA to spectral smile, which is translated in a greater uniformity across the image. In addition, the SSD mean values in the 2300 nm absorption window are 8.1 nm for EnMAP and 7.5 nm for PRISMA, which results in a greater number of

spectral bands for PRISMA (47 bands) within the 2300 nm window than for EnMAP (43 bands). This benefits PRISMA because it allows a greater number of measurements to characterize radiance spectra.

3.1.2. *Radiometric performance*

Figure 3 shows radiance spectral bands from similar central wavelenghts and equivalent adjacent band ratios from the same Turkmenistan area for EnMAP and PRISMA. The former uses a ratio between the 2104.9 nm band and 2096.0 nm band, while the latter uses one between the 2102.5 nm and 2094.4 nm band, which are the closest to EnMAP's. We use spectral bands located at the left shoulder of the 2300 nm methane band in order to avoid interference of the sought striping pattern with potential methane plumes in the imaged area. Both ratios show close-to-one values because the radiance spectra levels from adjacent bands is indeed very similar. In addition, although there is a temporal difference of 20 days, we can observe that there is little variation in the spatial patterns from one acquisition to the other. In order to evaluate the general variability, we show both ratios in a range of values comprising the mean and the standard deviation. We can observe a more pronounced striping pattern in EnMAP ratio, which would lead to a worse data uniformity for EnMAP than in the PRISMA case. This shows that applying the matched-filter method in a per-column basis is necessary for EnMAP. However, a more progressive pattern due to spectral smile can be observed in the PRISMA case, which confirms the spectral performance results of the previous section. Therefore, while EnMAP presents a more remarkable striping noise, PRISMA shows a higher spectral smile. In the future, further algorithms will be implemented in the EnMAP ground segment to remove low-frequent striping artifacts, so these results are only valid for the current delivered EnMAP data.

In Figure 4 we present the SNR spectra from Niger (EnMAP) and Sudan (PRISMA) datasets and the Niger radiance spectrum in the SWIR. Along the SWIR spectral range, EnMAP shows SNR values approximately twice as large as those of PRISMA in the 2300 nm absorption window. This, together with lower EnMAP FWHM values, will result in a lower retrieval precision error (Cusworth et al., 2018). In addition, we also scaled the EnMAP Niger SNR to the PRISMA Sudan radiance (L_{TOA}) following the proportionality with the square root of radiance and we found a negligible difference between the scaled and the not-scaled Niger SNR spectra that facilitates comparison between datasets.

3.1.3. *Methane retrieval performance*

We want to characterize and compare methane retrieval random errors from EnMAP and PRISMA missions. To do so, we will calculate the errors related to measurement noise and sensitivity to the background (Jacob et al., 2016) using relatively similar datasets with no methane emissions
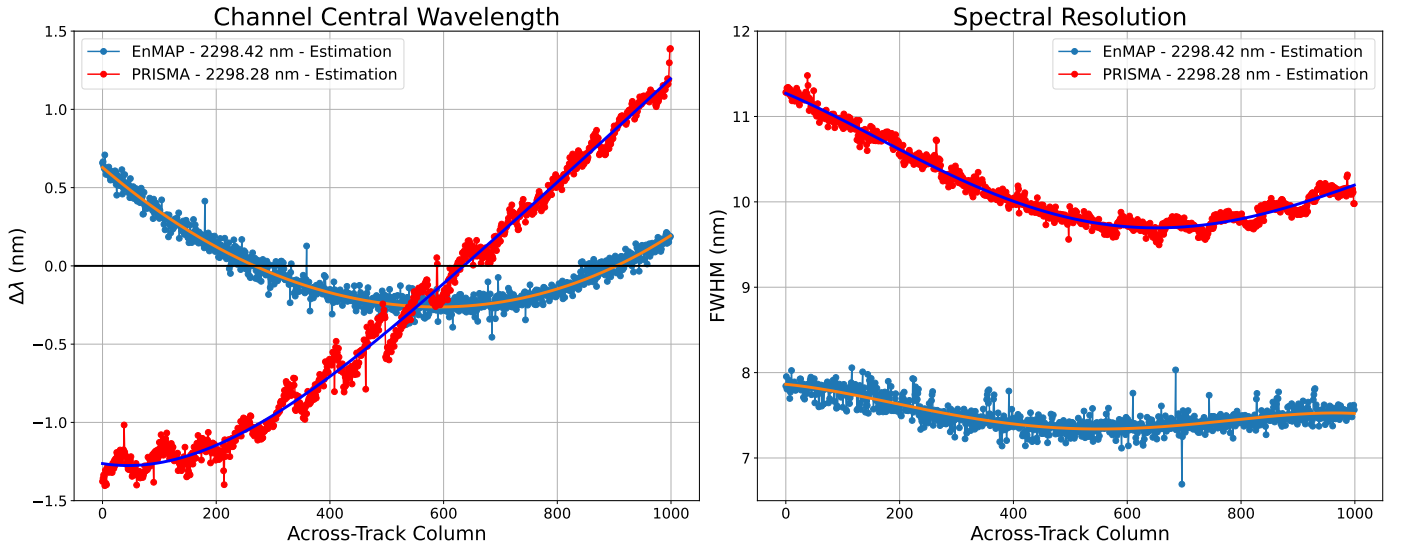
Fig. 2. Spectral smile (left) and spectral resolution (right) spectra in the #143 spectral band (2298.28 nm) from the PRISMA SWIR dataset in a Sudan site and in the #114 spectral band (2298.42 nm) from the EnMAP SWIR dataset in a Niger site.
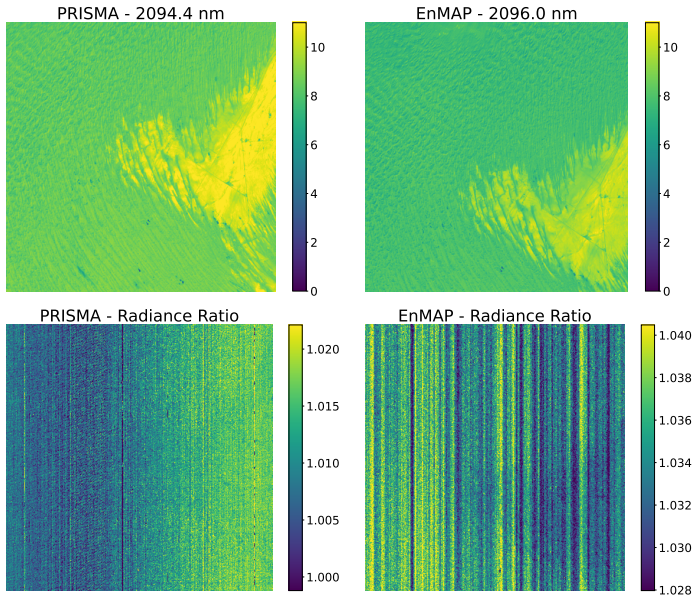

Fig. 3. ∼ 2095 nm radiance bands (top) and adjacent ratio images (bottom) from PRISMA (left) and EnMAP (right) datasets in the same Turkmenistan area. Ratio values are shown in the range of mean ± standard deviation from each ratio image.

in order not to disturb the study. Perfectly homogeneous datasets from the same site with high and equal radiance values would be ideal conditions to compare methane retrievals from both missions. However, it has been complicated to find datasets that meet these conditions because of the very short operational time of EnMAP (operative since November 2022). Instead, the Niger (EnMAP) and Sudan (PRISMA) datasets have been used to do this comparison because both present a similar spectrum shape along the 2300 nm window and homogeneous desert areas with high and similar radiance levels. This can be seen in Figure 5 where the spectral slope spectra, the *averaged radi-*

ance, and methane retrieval histograms from both datasets are shown. We can observe a similar spectral slope spectrum from the Niger and Sudan datasets, which indicates a similar surface composition from both sites. On the other hand, the averaged radiance is defined as the mean radiance within the 2300 nm absorption window and is representative of the radiance level in the matched-filter spectral range of application. Close standard deviation values from averaged radiance histograms confirm a similar surface variability, although there is a larger mean value relative difference ($\sim 10\%$) that questions whether the radiance values are similar enough to be comparable. In order to see the real impact on retrieval noise, the relative difference between averaged radiance values is propagated first to measurement noise and then to retrieval noise following Eq.5 and Eq.6. We find a negligible disturbance of methane retrieval of approximately 1%, which is consistent with the little difference between the not-scaled and scaled SNR Niger values from the previous section. Therefore, we can assume that methane retrievals from both datasets are comparable. The methane retrieval standard deviation can be interpreted as the total retrieval noise, which can be reformulated as the square root of the quadratic sum of surface variability and measurement noise contributions. Measurement noise contribution to methane retrieval noise is lower for Niger (10.4 ppb) than for Sudan (21.6 ppb). Moreover, although we have seen a similar surface variability, this contribution is also lower for the EnMAP Niger acquisition (13.1 ppb) than for the Sudan acquisition of PRISMA (19.4 ppb). We deduce that the lower FWHM from EnMAP can better separate background surface from methane absorption features, whereas the better SSD from PRISMA is not as relevant. Therefore, this confirms an EnMAP better retrieval performance that would lead to a greater capability to detect methane emissions.
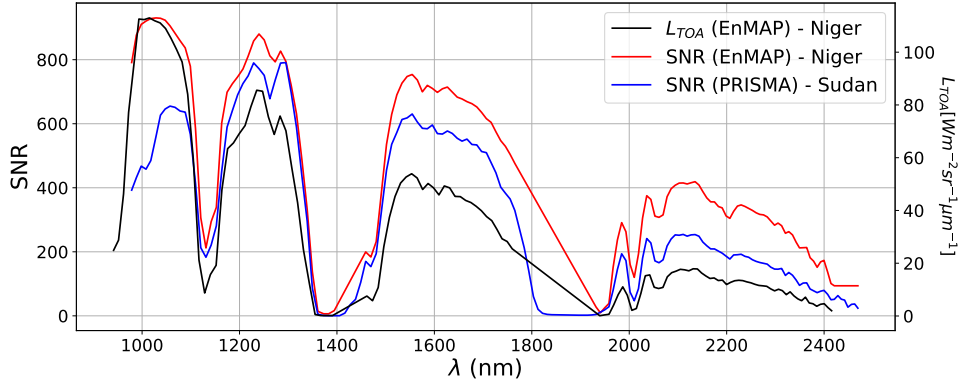
Fig. 4. TOA radiance (black) and SNR (red) spectra of an EnMAP dataset from a Niger area and a SNR spectrum of a PRISMA dataset from a Sudan area (blue).
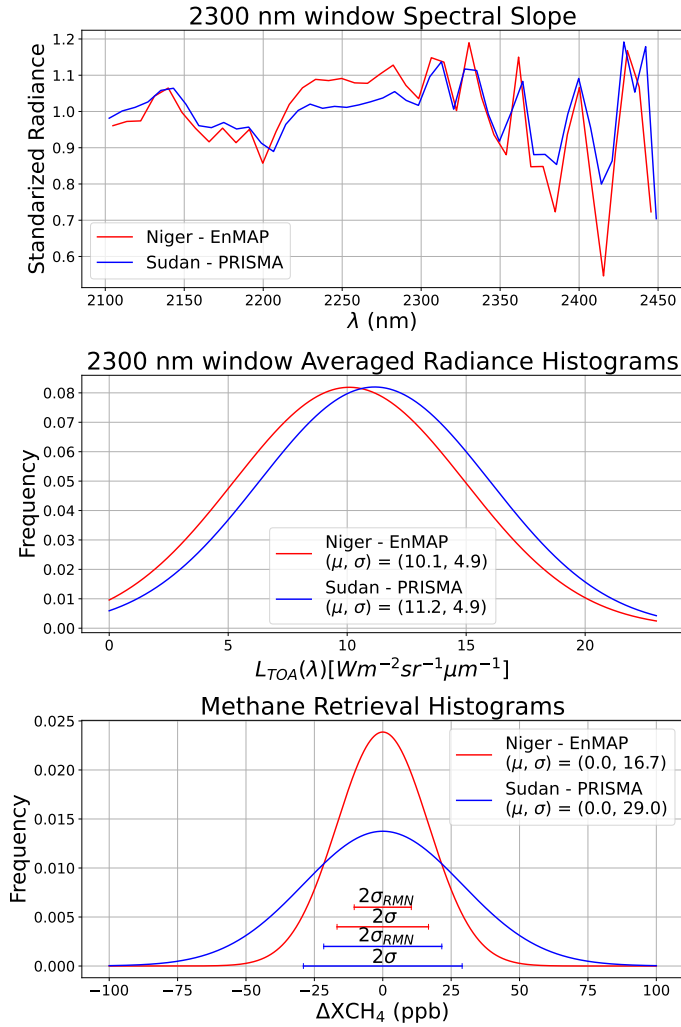
3.2. *Sample EnMAP plume detections from different source types*

Previous studies based on space-borne imaging spectrometers have detected methane plumes coming almost only from coal mining and O&G fields because their point-source nature results in more concentrated plumes that are easier to detect. However, the better retrieval performance of EnMAP has motivated us to search on sites where methane area-sources such as landfills are located. Additionally, we have also searched on O&G offshore areas, where the typical low radiance values in the SWIR damages plume detection. Offshore methane plumes have been detected from satellite (Irakulis-Loitxate et al., 2022a) because of the sunglint effect, which can be better exploited by EnMAP than by PRISMA thanks to its greater across-track pointing range.

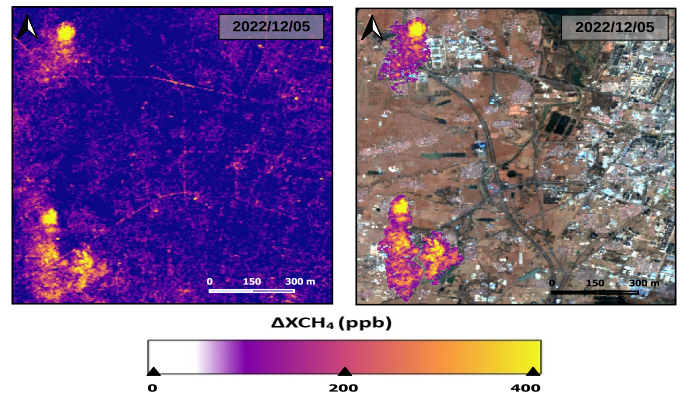### 3.2.1. *Coal mining in the Shanxi region (China)*

Fig. 6. Methane retrieval (left) and masked plumes overlaid on a true color image (right) of an EnMAP dataset from an coal mining area in the city of Shanxi (China).

In Figure 6 we show a methane retrieval from an EnMAP dataset in a coal mine region in the city of Shanxi (China). The low radiance levels and heterogeneity of this area generate less robust statistics and therefore results in a poorer

Fig. 5. 2300 nm absoprtion window spectral slope spectra (top), averaged radiance histograms (center), and methane retrieval histograms (bottom) from the Niger (EnMAP in red) and Sudan (PRISMA in blue) datasets. μ and σ of the center and bottom panels reflect the mean and standard deviation of their associated histograms, while σ_{RMN} reflects the measurement noise contribution to the methane retrieval error.

7

performance of the matched-filter. Additionally, there are surface structures spectrally similar to methane in the 2300 nm absorption window that cannot be separated and therefore are mistaken for methane. This leads to the existence of retrieval artifacts in the methane retrieval that reduces the potential for plume detection. However, the weak wind speed (0.7 ± 0.4 m/s) in this area at the acquisition time could have caused a greater concentration of the emissions, which allows us to observe three methane plumes coming from venting shafts that stand out from the background and the retrieval artifacts. Based on our mapping, we calculated a flux rate of 4.4 ± 0.8 t/h for the plume at the top, and flux rates of 5 ± 1 t/h and 3.8 ± 0.7 t/h for the two plumes at the bottom at the left and right side, respectively.

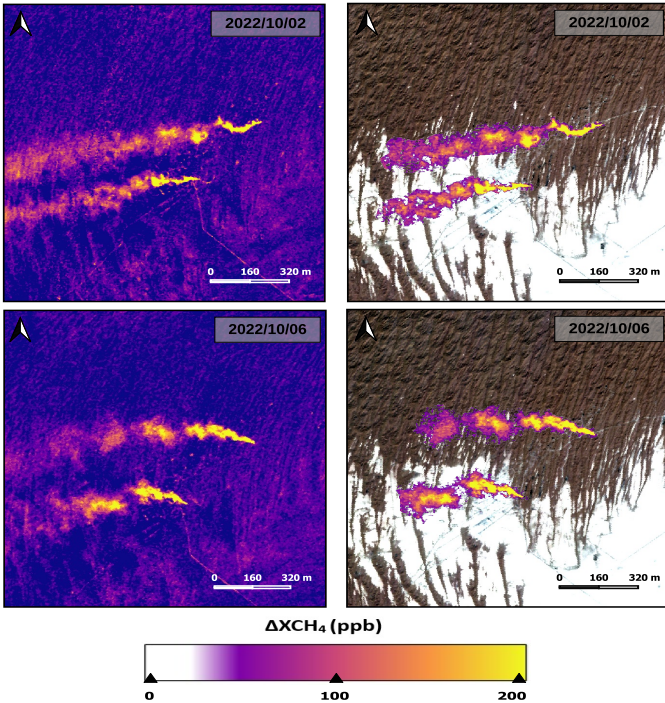### 3.2.2. *Onshore O&G extraction facilities in Turkmenistan*

Fig. 7. Methane retrieval (left) and masked plumes overlaid on a true color image (right) of an EnMAP dataset from an O&G field in Turkmenistan on 2022/10/02 (top) and on 2022/10/06 (bottom).

We have also been able to detect plumes from point-sources from onshore O&G facilities. Some of these emissions were located in an O&G field in Turkmenistan, where we observed methane plumes from the same two sources in two different days (see Figure 7). This shows the ability of satellite-based imaging spectroscopy missions such as EnMAP to monitor persistent methane sources. On the first day (2022/10/02) the flux rates values were 21 ± 9 t/h and 18 ± 8 t/h from the upper and lower source, respectively. On the other hand, on the second day (2022/10/06) the flux rates values were 13 ± 5 t/h and 14 ± 5 t/h from the upper and lower source, respectively. In addition, the area from this EnMAP dataset is bright and homogeneous, which results in a great performance of methane retrieval methods.

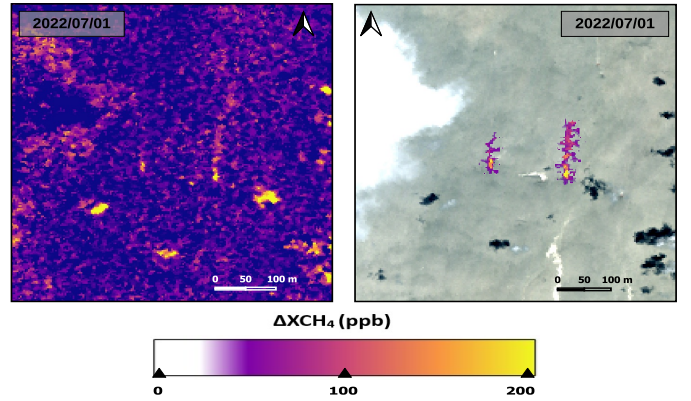### 3.2.3. *Offshore O&G platforms in the U.S. Gulf of Mexico*

Fig. 8. Methane retrieval (left) and masked plumes overlaid on a true color image (right) of an EnMAP dataset from an offshore O&G field in the U.S. Gulf of Mexico.

The high absorption of water in the SWIR spectral range reduces the detection of methane plumes. This will result in noisy methane retrievals because very low radiance values will imply measuring out of the sensor dynamic radiance range. However, there is a situation where the methane plume detection capability can improve for offshore datasets. This situation is the sunglint effect and it is defined as an increase of water reflectance when the angular configuration between the Sun and the detector approaches a mirror-like configuration. In this configuration the radiance reaching the detector will be much higher and therefore there would be a better chance of detecting methane emissions. This is why we look for offshore datasets with angular conditions as close as possible to the mirror-like configuration. The dataset angular configuration is determined by the Solar Azimuth Angle (SAA), the View Azimuth Angle (VAA), the Solar Zenith Angle (SZA), and the View Zenith Angle (VZA). In addition, we define the Relative Zenith Angle (RZA), which is expressed as RZA = SZA - VZA, and the Relative Azimuth Angle (RAA), which is expressed as RAA = SAA - VAA. Then, a perfect mirror-like configuration would result in $| \text{RZA} | = 0°$ and $| \text{RAA} | = 180°$. Across-track pointing from satellite contributes to meet these conditions and therefore a wider pointing range would translate into a higher probability of finding the sunglint effect. EnMAP has a larger avaliable across-track pointing range ($\pm 30°$) than PRISMA ($\pm 21°$), which makes EnMAP more suitable to detect offshore methane plumes.

Figure 8 shows two methane plumes from offshore O&G platforms in a U.S. Gulf of Mexico site. These platforms are potential emitters since methane emissions from this site have been already detected with airborne measurements (Ayasse, 2022) and also wind speed direction matches the plumes. We find that $| \text{RZA} |$ and $| \text{RAA} |$ are $23.88°$ and $19.71°$, respectively. These low values generate a close-to-sunglint situation that triggers a high level of radiance, which can be leveraged to detect methane plumes. We obtain a flux rate quantification of 0.93 ± 0.15 t/h and $1.1 \pm$

0.4 t/h for the plume on the left and on the right side of the image, respectively. Therefore, this study has shown emissions from offshore O&G platforms with unprecedented low flux rates around 1 t/h. This suggests that in EnMAP the detection limit under favorable conditions can be significantly low to monitor a broad number of offshore platforms.
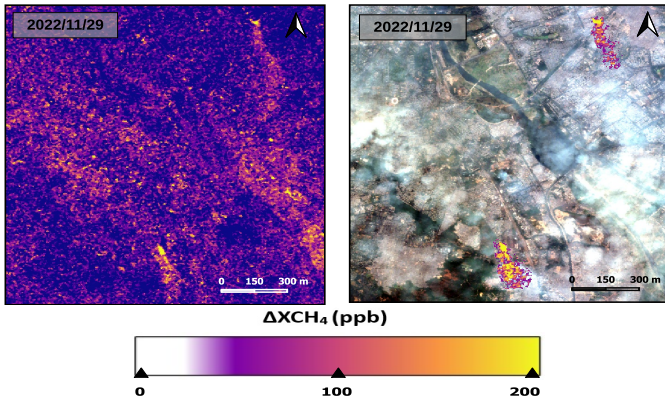
3.2.4. *Landfills in Delhi (India)*

Fig. 9. Methane retrieval (left) and masked plumes overlaid on a true color image (right) of an EnMAP dataset from a landfill area in Delhi (India).
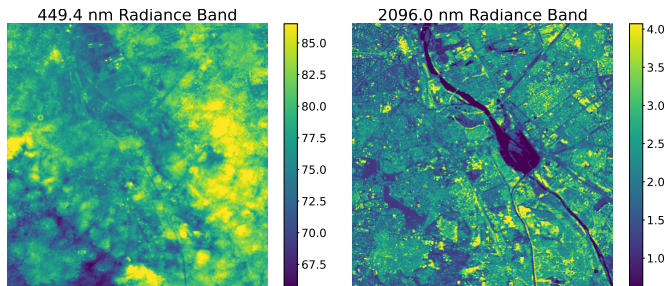

Fig. 10. 449.4 nm (left) and 2096.0 nm (right) radiance bands of an EnMAP dataset from a landfill area in Delhi (India).

Point-sources have been exploited to detect emissions because they can generate more concentrated plumes that lead to a greater absorption. Meanwhile, methane area-sources such as landfills release lower concentrated plumes, which makes these emissions difficult to detect. So far, there are few works done on the observation of methane emissions from landfills, which are mostly limited to medium-low resolution TROPOMI observations and detections from GHGSat - a constellation of private satellites specifically made to detect methane (Maasakkers et al., 2022; Lauvaux et al., 2022). Now, the higher SNR and lower FWHM values from EnMAP can better separate the methane features from the background, which could allow the detection of weaker methane plumes from landfills. In Figure 9 we can see two methane plumes originated from two landfills located in Delhi (India). We find that plume tails enhancements are almost at background level and the scene presents a high number of retrieval artifacts that disturb the detection of real methane plumes. However, both plumes match

wind direction, come from potential methane emitting areas, and show plume-like shapes. Additionally, although it seems that the scene is covered by clouds in the true color image, they can not be seen in the longer wavelengths. These clouds gradually disappear as the wavelength increases and therefore the SWIR radiance is insensitive to this cloud cover. We can observe this in Figure 10, where we can see that in the 449.4 nm VNIR band there is a remarkable cloud cover, while in a 2096.0 nm SWIR band this cover does not exist anymore. A possible explanation would be the presence of particles with a size comparable to VNIR and SWIR wavelengths such as in smoke or haze that interact with radiation following the Mie scattering. A high concentration of pollutants of this size is registered in the acquisition date in Delhi (PIB Delhi, 2022), where the landfills are located, and therefore it would explain the lack of visibility across the scene. Thus, since the 2300 nm window is insensitive to these clouds, we have been able to detect these plumes, which establishes the possibility to detect methane area-source emissions from EnMAP datasets. Additionally, flux rate values of 1.8 ± 0.5 t/h and 2.8 ± 0.7 t/h are calculated for the plumes located on the upper and lower part of the scene, respectively. These calculations are made following an equation calibrated to point-source emissions, which could not be valid for area-source emissions. Nevertheless, because of their large size we can assume that plume dimensions are much higher than the emitting area size and therefore we can approximate these cases to point-source emissions.

3.2.5. *Plumes detected around the world*

Together to the ones already exposed, in Figure 11 we illustrate different plumes detected around the world with their corresponding flux rate values. This shows the EnMAP capability to detect methane plumes in a wide range of different scenarios (variable atmospheric conditions, radiance levels, surface composition, and methane emission flux rates). In addition to the plumes shown in previous sections, we find a plume from a Permian Basin (U.S.) site, two other emissions from an O&G field in Algeria, and four more plumes in an O&G field in Turkmenistan. Moreover, we find two plumes from the same pumping station (O&G facility) in Iran, which shows another case of the EnMAP ability to monitor persistent emissions. Additionally, we can see that the flux rates of the different plumes range from approximately 1 to 20 t/h. The bigger emissions were originated in the Turkemistan O&G fields and China coal mines. On the other hand, the lowest emission was found coming from a offshore O&G platform in the U.S. GoM. However, a detection limit lower than 1 t/h is expected since plumes with a flux rate of 0.5 t/h were found with PRISMA (Irakulis-Loitxate et al., 2021).
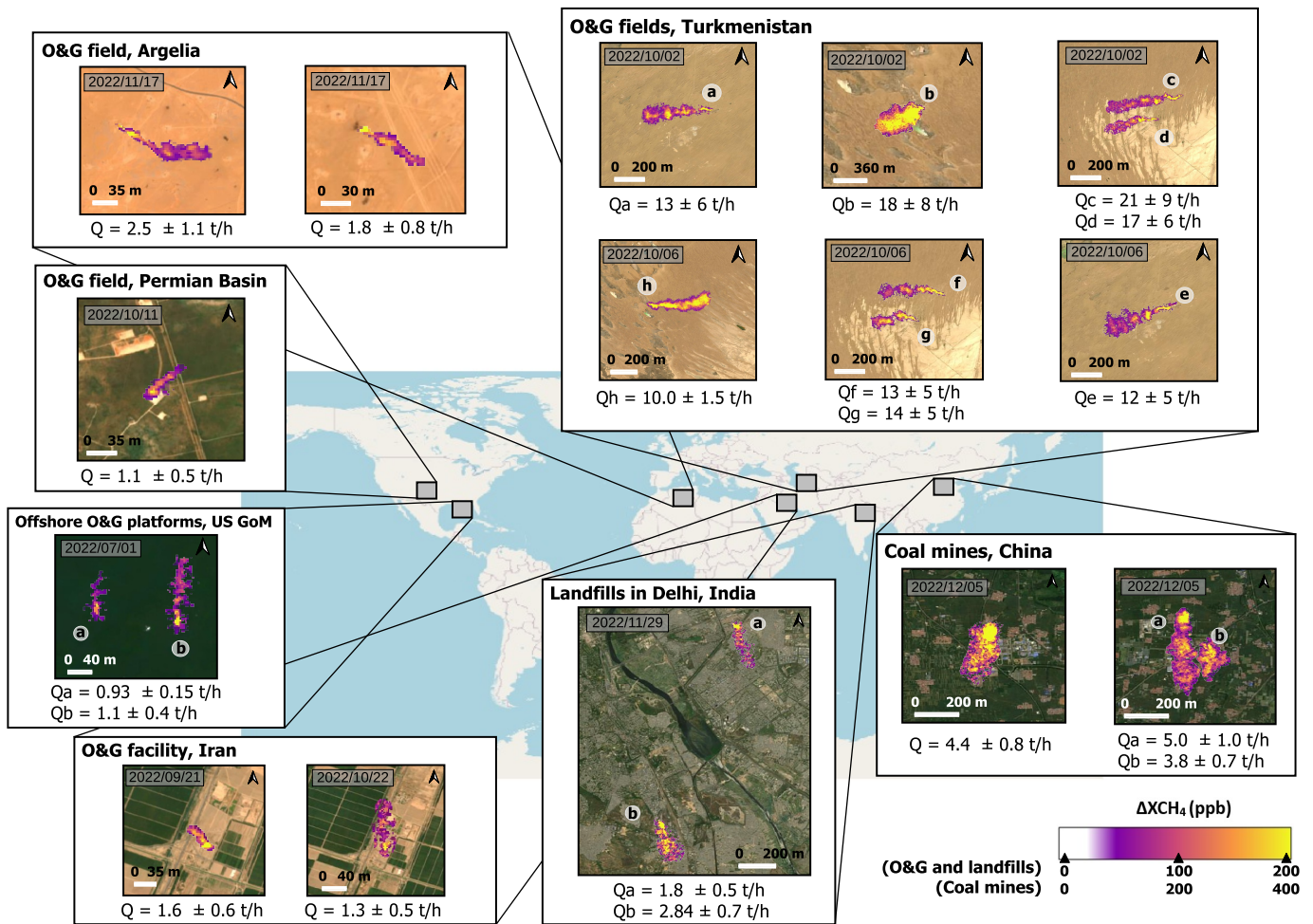
Fig. 11. Masked methane plumes around the world linked to their flux rate value and overlaid on Google Earth true-color imagery.

4. Conclusions

In this work we have studied the spectral and radiometric performance of EnMAP in order to assess their impact on methane retrievals taking PRISMA as a benchmark. In addition, EnMAP plumes coming from different emission sectors are shown to illustrate its ability to map methane emissions.

The spectral and radiometric performance of EnMAP is studied in the 2300 nm absorption window, where the matched-filter method is applied. Results show that PRISMA presents a better SSD and striping noise, while EnMAP presents better FWHM, SNR and, spectral smile. Striping noise and spectral smile are avoided applying the matched-filter method in a per-column basis. SSD is lower for PRISMA and therefore it presents a higher number of bands to characterize the radiance spectra. However, results show that the lower FWHM and higher SNR from EnMAP in the 2300 nm absorption window derives in a lower retrieval noise. Moreover, methane retrievals from datasets around the world demonstrate the capability of EnMAP to detect methane plumes in a wide range of scenarios. In addition to point-source emissions from onshore O&G facilities and coal mines, we have also been able to detect emissions from offshore O&G facilities and landfills. The higher across-track pointing range from EnMAP makes it easier to find close-to-sunglint situations where there is a better chance to detect emissions in offshore scenarios and its higher sensibility to methane makes it more suitable to detect area-sources.

CRediT authorship contribution statement

Javier Roger: Conceptualization, Methodology, Formal Analysis, Investigation, Writing - original draft, Writing - review & editing. **Itziar Irakulis-Loitxate**: Resources, Writing - review. **Adriana Valverde**: Resources, Figures, Writing - review & editing. **Javier Gorroño**: Methodology, Writing - review. **Sabine Chabrillat**: Resources, Writing - review. **Maximmilian Brell**: Resources, Writing - review. **Luis Guanter**: Conceptualization, Methodology, Formal Analysis, Writing - review.

Declaration of Competing Interest

The authors declare that they have no known competing financial interests or personal relationships that could have appeared to influence the work reported in this paper.

Acknowledgment

The authors thank the Italian Space Agency and the DLR Space Agency for the PRISMA and EnMAP data used in this work, respectively.

Data availability

Data will be made available on request.

References

Cusworth, D. H., Jacob, D. J., Sheng, J.-X., Benmergui, J., Turner, A. J., Brandman, J., White, L., Randles, C. A., 2018. Detecting high-emitting methane sources in oil/gas fields using satellite observations. Atmospheric Chemistry and Physics 18 (23), 16885–16896.
URL https://acp.copernicus.org/articles/18/16885/2018/

Cusworth, D. H., Jacob, D. J., Varon, D. J., Chan Miller, C., Liu, X., Chance, K., Thorpe, A. K., Duren, R. M., Miller, C. E., Thompson, D. R., Frankenberg, C., Guanter, L., Randles, C. A., 2019. Potential of next-generation imaging spectrometers to detect and quantify methane point sources from space. Atmospheric Measurement Techniques 12 (10), 5655–5668.
URL https://amt.copernicus.org/articles/12/5655/2019/

Dennison, P. E., Thorpe, A. K., Roberts, D. A., Green, R. O., 2013. Modeling sensitivity of imaging spectrometer data to carbon dioxide and methane plumes. 2013 5th Workshop on Hyperspectral Image and Signal Processing: Evolution in Remote Sensing (WHISPERS), 1–4.

Du, H., Xu, J., Yin, Z., Chai, M., Sun, D., 2022. Dark current noise correction method based on dark pixels for lwir qwip detection systems. Applied Sciences 12 (24).
URL https://www.mdpi.com/2076-3417/12/24/12967

Duren, R., Thorpe, A., Foster, K., Rafiq, T., Hopkins, F., Yadav, V., Bue, B., Thompson, D., Conley, S., Colombi, N., Frankenberg, C., McCubbin, I., Eastwood, M., Falk, M., Herner, J., Croes, B., Green, R., Miller, C., 11 2019. California's methane super-emitters. Nature 575, 180–184.

Eismann, M., 2012. Hyperspectral Remote Sensing. Vol. PM210 of SPIE Press Monograph. Society of Photo Optical.

Foote, M. D., Dennison, P. E., Thorpe, A. K., Thompson, D. R., Jongaramrungruang, S., Frankenberg, C., Joshi, S. C., 2020. Fast and accurate retrieval of methane concentration from imaging spectrometer data using sparsity prior. IEEE Transactions on Geoscience and Remote Sensing 58 (9), 6480–6492.

Frankenberg, C., Thorpe, A. K., Thompson, D. R., Hulley, G., Kort, E. A., Vance, N., Borchardt, J., Krings, T., Gerilowski, K., Sweeney, C., Conley, S., Bue, B. D., Aubrey, A. D., Hook, S., Green, R. O., 2016. Airborne methane remote measurements reveal heavy-tail flux distribution in four corners region. Proceedings of the National Academy of Sciences 113 (35), 9734–9739.
URL https://www.pnas.org/content/113/35/9734

Gege, P., Fries, J., Haschberger, P., Schötz, P., Schwarzer, H., Strobl, P., Suhr, B., Ulbrich, G., Vreeling, W. J., 2009. Calibration facility for airborne imaging spectrometers. ISPRS Journal of Photogrammetry and Remote Sensing 64 (4), 387–397.

Gordon, I., Rothman, L., Hill, C., Kochanov, R., Tan, Y., Bernath, P., Birk, M., Boudon, V., Campargue, A., Chance, K., Drouin, B., Flaud, J.-M., Gamache, R., Hodges, J., Jacquemart, D., Perevalov, V., Perrin, A., Shine, K., Smith, M.-A., Tennyson, J., Toon, G., Tran, H., Tyuterev, V., Barbe, A., Császár, A., Devi, V., Furtenbacher, T., Harrison, J., Hartmann, J.-M., Jolly, A., Johnson, T., Karman, T., Kleiner, I., Kyuberis, A., Loos, J., Lyulin, O., Massie, S., Mikhailenko, S., Moazzen-Ahmadi, N., Müller, H., Naumenko, O., Nikitin, A., Polyansky, O., Rey, M., Rotger, M., Sharpe, S., Sung, K., Starikova, E., Tashkun, S., Auwera, J. V., Wagner, G., Wilzewski, J., Wcisło, P., Yu, S., Zak, E., 2017. The hitran2016 molecular spectroscopic database. Journal of Quantitative Spectroscopy and Radiative Transfer 203, 3–69, hITRAN2016 Special Issue.
URL https://www.sciencedirect.com/science/article/pii/S0022407317301073

Green, R., 2021. The nasa earth surface mineral dust source investigation. 43rd COSPAR Scientific Assembly. Held 28 January-4 February 43, 37.

Green, R. O., Feb 1998. Spectral calibration requirement for earth-looking imaging spectrometers in the solar-reflected spectrum. Appl. Opt. 37 (4), 683–690.
URL https://opg.optica.org/ao/abstract.cfm?URI=ao-37-4-683

Guanter, L., Irakulis-Loitxate, I., Gorroño, J., Sánchez-García, E., Cusworth, D. H., Varon, D. J., Cogliati, S., Colombo, R., 2021. Mapping methane point emissions with the prisma spaceborne imaging spectrometer. Remote Sensing of Environment 265, 112671.
URL https://www.sciencedirect.com/science/article/pii/S0034425721003916

Guanter, L., Kaufmann, H., Segl, K., Foerster, S., Rogass, C., Chabrillat, S., Kuester, T., Hollstein, A., Rossner, G., Chlebek, C., et al., Jul 2015. The EnMAP Spaceborne Imaging Spectroscopy Mission for Earth Observation. Remote Sensing 7 (7), 8830–8857.
URL http://dx.doi.org/10.3390/rs70708830

Guanter, L., Segl, K., Sang, B., Alonso, L., Kaufmann, H.,

Moreno, J., Jul 2009. Scene-based spectral calibration assessment of high spectral resolution imaging spectrometers. Opt. Express 17 (14), 11594–11606.
URL https://opg.optica.org/oe/abstract.cfm?URI=oe-17-14-11594

Hersbach, H., Bell, B., Berrisford, P., Biavati, G., Horányi, A., Sabater, J. M., Nicolas, J., Peubey, C., Radu, R., Rozum, I., Schepers, D., Simmons, A., Soci, C., Dee, D., Thépaut, J.-N., 2018. ERA5 hourly data on single levels from 1959 to present. Copernicus Climate Change Service (C3S) Climate Data Store (CDS). Accessed: 07-02-2023), 10.24381/cds.adbb2d47.

Irakulis-Loitxate, I., Gorroño, J., Zavala-Araiza, D., Guanter, L., 2022a. Satellites detect a methane ultra-emission event from an offshore platform in the gulf of mexico. Environmental Science & Technology Letters 9 (6), 520–525.
URL https://doi.org/10.1021/acs.estlett.2c00225

Irakulis-Loitxate, I., Guanter, L., Liu, Y.-N., Varon, D. J., Maasakkers, J. D., Zhang, Y., Chulakadabba, A., Wofsy, S. C., Thorpe, A. K., Duren, R. M., Frankenberg, C., Lyon, D. R., Hmiel, B., Cusworth, D. H., Zhang, Y., Segl, K., Gorroño, J., Sánchez-García, E., Sulprizio, M. P., Cao, K., Zhu, H., Liang, J., Li, X., Aben, I., Jacob, D. J., 2021. Satellite-based survey of extreme methane emissions in the permian basin. Science Advances 7 (27).
URL https://advances.sciencemag.org/content/7/27/eabf4507

Irakulis-Loitxate, I., Guanter, L., Maasakkers, J. D., Zavala-Araiza, D., Aben, I., 2022b. Satellites detect abatable super-emissions in one of the world's largest methane hotspot regions. Environmental Science & Technology 56 (4), 2143–2152, pMID: 35102741.
URL https://doi.org/10.1021/acs.est.1c04873

Jacob, D. J., Turner, A. J., Maasakkers, J. D., Sheng, J., Sun, K., Liu, X., Chance, K., Aben, I., McKeever, J., Frankenberg, C., 2016. Satellite observations of atmospheric methane and their value for quantifying methane emissions. Atmospheric Chemistry and Physics 16 (22), 14371–14396.
URL https://acp.copernicus.org/articles/16/14371/2016/

Joyce, P., Ruiz Villena, C., Huang, Y., Webb, A., Gloor, M., Wagner, F. H., Chipperfield, M. P., Barrio Guilló, R., Wilson, C., Boesch, H., 2022. Using a deep neural network to detect methane point sources and quantify emissions from prisma hyperspectral satellite images. EGUsphere 2022, 1–22.
URL https://egusphere.copernicus.org/preprints/egusphere-2022-924/

Köhler, P., Guanter, L., Joiner, J., 2015. A linear method for the retrieval of sun-induced chlorophyll fluorescence from gome-2 and sciamachy data. Atmospheric Measurement Techniques 8 (6), 2589–2608.
URL https://amt.copernicus.org/articles/8/2589/2015/

Lauvaux, T., Giron, C., Mazzolini, M., d'Aspremont, A., Duren, R., Cusworth, D., Shindell, D., Ciais, P., 2022. Global assessment of oil and gas methane ultra-emitters. Science 375 (6580), 557–561.
URL https://www.science.org/doi/abs/10.1126/science.abj4351

Loizzo, R., Guarini, R., Longo, F., Scopa, T., Formaro, R., Facchinetti, C., Varacalli, G., 07 2018. Prisma: The italian hyperspectral mission. pp. 175–178.

Luo, B., Yan, L., Yang, F., 2010. Research of noise suppression for cmos image sensor. In: 2010 International Conference on Measuring Technology and Mechatronics Automation. Vol. 2. pp. 1100–1103.

Maasakkers, J. D., Varon, D. J., Elfarsdóttir, A., McKeever, J., Jervis, D., Mahapatra, G., Pandey, S., Lorente, A., Borsdorff, T., Foorthuis, L. R., Schuit, B. J., Tol, P., van Kempen, T. A., van Hees, R., Aben, I., 2022. Using satellites to uncover large methane emissions from landfills. Science Advances 8 (32), eabn9683.
URL https://www.science.org/doi/abs/10.1126/sciadv.abn9683

Ming, T., Li, W., Yuan, Q., Davies, P., de Richter, R., Peng, C., Deng, Q., Yuan, Y., Caillol, S., Zhou, N., 2022. Perspectives on removal of atmospheric methane. Advances in Applied Energy 5, 100085.
URL https://www.sciencedirect.com/science/article/pii/S2666792422000038

Molod, A., Takacs, L., Suarez, M., Bacmeister, J., Song, I.-S., Eichmann, A., 2012. he GEOS-5 Atmospheric General Circulation Model: Mean Climate and Development from MERRA to Fortuna. https://portal.nccs.nasa.gov/datashare/gmao/geos-fp/das/, nASA TM-2012-104606, 2012.

Myhre, G., Shindell, D., Bréon, F., Collins, W., Fuglestvedt, J., Huang, J., Koch, D., Lamarque, J., Lee, D., Mendoza, B., et al., 2013. Climate change 2013: the physical science basis. contribution of working group i to the fifth assessment report of the intergovernmental panel on climate change.

Omara, M., Zavala-Araiza, D., Lyon, D., Hmiel, B., Roberts, K., Hamburg, S., 2022. Methane emissions from us low production oil and natural gas well sites. Nature Communications 13.
URL https://doi.org/10.1038/s41467-022-29709-3

PIB Delhi, 2022. 2022 - Air Quality Perspective in Delhi. Accessed: 01-03-2023), Ministry of Environment, Forest and Climate Change.
URL https://pib.gov.in/PressReleasePage.aspx?PRID=1888090

Thompson, D. R., Leifer, I., Bovensmann, H., Eastwood, M., Fladeland, M., Frankenberg, C., Gerilowski, K., Green, R. O., Kratwurst, S., Krings, T., Luna, B., Thorpe, A. K., 2015. Real-time remote detection and measurement for airborne imaging spectroscopy: a case study with methane. Atmospheric Measurement Techniques 8 (10), 4383–4397.

URL https://amt.copernicus.org/articles/8/4383/2015/

Thompson, D. R., Thorpe, A. K., Frankenberg, C., Green, R. O., Duren, R., Guanter, L., Hollstein, A., Middleton, E., Ong, L., Ungar, S., 2016. Space-based remote imaging spectroscopy of the aliso canyon ch4 superemitter. Geophysical Research Letters 43 (12), 6571–6578.
URL https://agupubs.onlinelibrary.wiley.com/doi/abs/10.1002/2016GL069079

Tsai, F., Chen, W., 2008. Striping noise detection and correction of remote sensing images. IEEE Transactions on Geoscience and Remote Sensing 46 (12), 4122–4131.

UNEP, 2021. Global Methane Assessment: Benefits and Costs of Mitigating Methane Emissions. https://www.unep.org/resources/report/global-methane-assessment-benefits-and-costs-mitigating-methane-emissions.

Varon, D. J., Jacob, D. J., McKeever, J., Jervis, D., Durak, B. O. A., Xia, Y., Huang, Y., 2018. Quantifying methane point sources from fine-scale satellite observations of atmospheric methane plumes. Atmospheric Measurement Techniques 11 (10), 5673–5686.
URL https://amt.copernicus.org/articles/11/5673/2018/

Zavala-Araiza, D., Alvarez, R., Lyon, D., Allen, D., Marchese, A., Zimmerle, D., Hamburg, S., 01 2017. Superemitters in natural gas infrastructure are caused by abnormal process conditions. Nature Communications 8, 14012.